Nontrivial spin texture of the coaxial Dirac cones on the surface of topological crystalline insulator SnTe

Yung Jui Wang,[1,2] Wei-Feng Tsai,[3] Hsin Lin,[1] Su-Yang Xu,[4] M. Neupane,[4] M. Z. Hasan,[4] and A. Bansil[1]
[1]*Department of Physics, Northeastern University, Boston, Massachusetts 02115, USA*
[2]*Advanced Light Source, Lawrence Berkeley National Laboratory, Berkeley, California 94305, USA*
[3]*Department of Physics, National Sun Yat-sen University, Kaohsiung 80424, Taiwan*
[4]*Joseph Henry Laboratory, Department of Physics, Princeton University, Princeton, New Jersey 08544, USA*
(Received 30 April 2013; published 25 June 2013)

We present first-principles calculations of the nontrivial surface states and their spin textures in the topological crystalline insulator SnTe. The surface state dispersion on the [001] surface exhibits four Dirac cones centered along the intersection of the mirror plane and the surface plane. We propose a simple model of two interacting coaxial Dirac cones to describe both the surface state dispersion and the associated spin texture. The out-of-plane spin polarization is found to be zero due to the crystalline and time-reversal symmetries. The in-plane spin texture shows helicity with some distortion due to the interaction of the two coaxial Dirac cones, indicating a nontrivial mirror Chern number of -2, distinct from the value of -1 in a Z_2 topological insulator such as Bi/Sb alloys or Bi_2Se_3. The surface state dispersion and its spin texture would provide an experimentally accessible signature for determining the nontrivial mirror Chern number.

DOI: 10.1103/PhysRevB.87.235317 PACS number(s): 73.43.Cd, 71.20.Nr, 73.20.At

I. INTRODUCTION

Since the discovery of time-reversal symmetry protected topological quantum states in two-dimensional (2D) Hg(Cd)Te-based quantum well structures, and subsequently that of the Z_2 three-dimensional (3D) topological insulators,[1–7] an enormous effort has been dedicated toward finding other novel materials which could support nontrivial topological states. One particularly fruitful recent direction has been to explore quantum states in condensed matter systems, which are protected by the symmetries of the lattice, leading to the so-called topological crystalline insulators (TCIs).[8] A practical realization of a TCI has been the prediction of SnTe with an ideal rocksalt structure in which the mirror symmetry of the lattice ensures the existence of robust metallic surface states.[9] This theoretical prediction was verified quickly via angle-resolved photoemission experiments on $Pb_{1-x}Sn_xTe$ (Refs. 10 and 11) and $Pb_{1-x}Sn_xSe$.[12] Recall that a Z_2 topological insulator such as Bi_2Se_3/Te_3, which is protected by time-reversal symmetry, contains a single Dirac cone at the center of the [111] surface plane, exhibiting a linear dispersion and chiral spin texture predicted theoretically as well as observed experimentally.[7] In contrast to the 3D Z_2 topological insulators, however, a TCI protected by mirror symmetry contains an even number of Dirac cones on crystal surfaces symmetric about the [110] mirror planes, and its topologically nontrivial state is characterized by a nonzero mirror Chern number.[9,13] The interest in understanding the bizarre surface states and their spin textures in SnTe, the pristine phase of an archetype TCI, is thus obvious, both in its own right and as a way of gaining insight into the properties of related substitutional compounds.

In this work, we report first-principles calculations to investigate the [001] surface states of SnTe in rocksalt structure. By including the spin-orbit coupling, two gapless Dirac cones centered along $\bar{\Gamma}\bar{X}$ [the other two lie along $\bar{\Gamma}\bar{Y}$],[14] a mirror line of the crystal symmetry, are found in the surface spectrum, a result of the nontrivial band topology due to crystal symmetry. We examine the complicated surface band characters as well as the nontrivial spin textures and propose a simple model which consists of two interacting coaxial Dirac cones centered at $\bar{X}$. When the interaction between the two coaxial Dirac cones is turned on, the two surface bands avoid each other and a gap opens up except on the mirror line, forming the gapless Dirac cones centered along $\bar{\Gamma}\bar{X}$. While the out-of-plane spin polarization vanishes due to C_{4v} symmetry as well as the superposition of the mirror and time-reversal symmetries, the in-plane spin textures show helicity with some distortion due the interaction of the two Dirac cones. The overall spin texture reveals the nontrivial mirror Chern number with the value of -2, which is distinct from that of -1 in Z_2 topological insulators such as Bi/Sb alloy and Bi_2Se_3.[6,13,15] The surface state dispersion and the associated spin texture would provide an experimentally accessible signature to determine the nontrivial mirror Chern number.

II. BAND-STRUCTURE CALCULATIONS

We first extract both the electronic band structure and the spin texture of the SnTe surface states from first-principles calculations, which were carried out within the framework of the density functional theory (DFT) using the projector augmented wave method[16] as implemented in the VASP package.[17] The generalized gradient approximation (GGA)[18] was used to model exchange-correlation effects. The spin orbital coupling (SOC) is included in the self-consistent cycles. The surface was modeled by periodically repeated slabs of 33 atomic layer thickness with 13-Å-wide vacuum regions using a $12 \times 12 \times 1$ Monkhorst-Pack k-point mesh over the Brillouin zone (BZ) with 208-eV cutoff energy. The room temperature crystal structure of SnTe in an ideal sodium chloride structure was used to construct the slab without a rhombohedral distortion. The experimental lattice constant of SnTe with a value of 6.327 Å was used.[19] The self-consistent

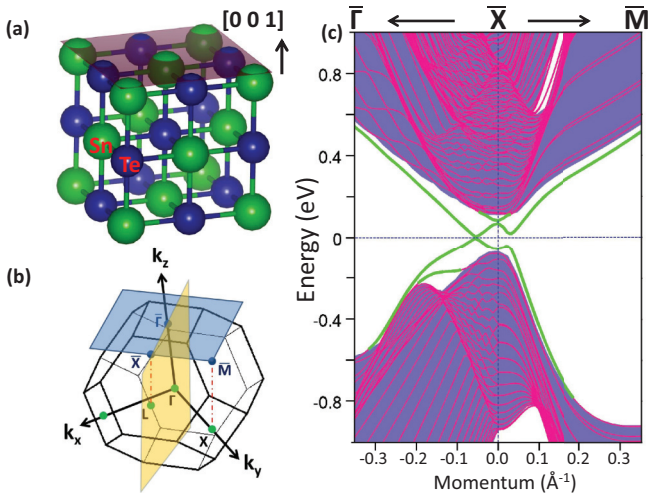

FIG. 1. (Color online) Crystal structure and surface bands of SnTe. (a) Rocksalt crystal structure of SnTe. A [001] surface plane is shown. (b) fcc Brillouin zone (BZ) of SnTe and the [001] surface BZ. The [1 −1 0] mirror plane crosses the 2D surface BZ along $\bar{\Gamma}\bar{X}$. (c) Electronic structure of SnTe [001] surface around $\bar{X}$. The surface bands are indicated by thick green lines and bulk bands by the shaded purple area. A Dirac point of the surface state appears along the $\bar{\Gamma}\bar{X}$ direction, while the surface band is gapped along $\bar{X}\bar{M}$.

Bloch wave functions associated with the surface states were decomposed into cubic spherical harmonic orbitals and projected onto various atomic sites. For each atomic site in SnTe, we obtained the charge density and the three components of the spin direction from the expectation values of the x, y, and z Pauli matrices.

In order to clarify the relevant structural aspects, SnTe in an ideal sodium chloride fcc crystal structure is shown in Fig. 1(a). Figure 1(b) shows the fcc bulk BZ as well as the [001] surface BZ. The high-symmetry points Γ(0,0,0), L(0.5,0.5,0.5), and X(1,0,0) in the bulk BZ are projected on the $\bar{\Gamma}$(0,0), $\bar{X}$(0.5,0), and $\bar{M}$(0.5,0.5) in the surface BZ, respectively. Coordinates are given in units of $2\pi/a_b$ for points in the bulk BZ and $2\pi/a$ for those in the surface BZ where a_b (a) is the bulk (surface) lattice constant. The relation $a_b = \sqrt{2}a$ generally holds for the [001] surface of an fcc crystal. In order to make a distinction between the two equivalent points (0.5,0) and (0,0.5) in the surface BZ, $\bar{Y}$ is defined as (0,0.5). While Γ, L, and X are time-reversal invariant points in the bulk BZ, $\bar{\Gamma}$, $\bar{X}$, $\bar{Y}$, and $\bar{M}$ are the only four time-reversal invariant points in the surface BZ. The surface Dirac points, if any, which lie on these four points are protected by time-reversal symmetry. The [1 −1 0] mirror plane is perpendicular to the [001] surface plane and projected onto the surface BZ along the $\bar{\Gamma}\bar{X}$ direction. The surface Dirac points, if any, which lie on the mirror line along the $\bar{\Gamma}\bar{X}$ are protected by mirror symmetry. The projected bulk band structure along the high-symmetry lines $\bar{\Gamma}$-$\bar{X}$-$\bar{M}$ is shown in Fig. 1(c) by the purple area. The surface bands are highlighted by thick green lines, isolated from other bulk bands. There is a gapless Dirac cone with the Dirac point sitting along $\bar{\Gamma}$-$\bar{X}$ on the two sides of the $\bar{X}$ point at the Fermi level, while the surface states along $\bar{X}$-$\bar{M}$ are gapped.

The complicated surface states of SnTe can be understood by a simpler picture, which consists of two Dirac cones. Figure 2(a) shows two coaxial Dirac cones centered at the $\bar{X}$ point. The $\bar{X}$ and $\bar{Y}$ points, i.e., (0.5, 0) and (0, 0.5), are equivalent and we concentrate on the one at (0.5,0) hereafter. These two Dirac cones carry different band characters and can be distinguished through an analysis of the wave functions of the Sn and Te atoms on the surface layers of the [001] slab. The nature of the differences in potentials of the Sn and Te atoms separates the two Dirac cones in energy vertically, as shown in Fig. 2(a). If there are no interactions between the two Dirac cone states, the two Dirac cones will intersect each other in the 2D surface BZ in an ellipse, which only intersects the mirror line along $\bar{\Gamma}$-$\bar{X}$ (blue line) with two points on the two sides of the $\bar{X}$ point. In Fig. 2(b), when the interaction between the two Dirac cones is turned on, a gap opens up along the elliptical overlap region of the two Dirac cones, except at the two points protected by the mirror symmetry.

In order to trace the band character of the SnTe surface states, we decompose their charge distribution into Sn and Te partial contributions, presented in Figs. 2(c)–2(f). For the surface valence states [Fig. 2(c)], we find that the Sn fraction is dominant within an elliptical region between the two Dirac points and centered at the $\bar{X}$ point, while in Fig. 2(d) the Te fraction is larger outside this region. But for the conduction surface states [Figs. 2(e) and 2(f)], this trend between the partial contributions from Se and Te atoms is reversed. To enhance visual clarity, we patch the charge fraction map onto the energy dispersion in Fig. 2(g). These results of first-principles calculations qualitatively agree with the picture of two interacting Dirac cones shown in Fig. 2(b) and allow us to attribute the origin of the two coaxial Dirac cones to distinct atomic orbitals. One of the cones with an opening to the high-energy side is more Sn-like with a p_z orbital, while the other cone with an opening to the low-energy side is more Te-like with a p_x orbital. The Sn-like cone has the $\bar{X}$-point Dirac point lower in energy than that of the Te-like cone.

In Fig. 3 we plot surface band energies using a color scale and the associated constant energy contours, together with the in-plane spin texture. The spin direction of each state was obtained here by calculating the expectation values of the Pauli matrices from the first six atomic layers from the top surface of the SnTe slab. For the valence surface states shown in Fig. 3(b), the highest energy state is located at the Dirac points lying along the $\bar{\Gamma}\bar{X}$ mirror line. The constant energy contours close to the Dirac points are seen not to be of a perfect circular shape, which implies an anisotropic Fermi velocity around the Dirac points. Between the two Dirac points, an energy valley is centered at the $\bar{X}$ point.

The energy contours exhibit a Lifshitz transition.[9] As we go to energies below the Fermi energy, the constant energy surface changes its topology. The two disconnected hole pockets next to the $\bar{X}$ point at high energy become a large hole and a small electron pocket, both centered at the $\bar{X}$ point at low energy. In the two coaxial Dirac cones, the large hole pocket is associated with the Te-like lower Dirac cone while the small electron pocket is associated with the Sn-like upper Dirac cone. A similar change in the Fermi surface topology occurs in the conduction surface bands [Fig. 3(a)]. At high energies above the interaction region, the large electron and small hole pocket

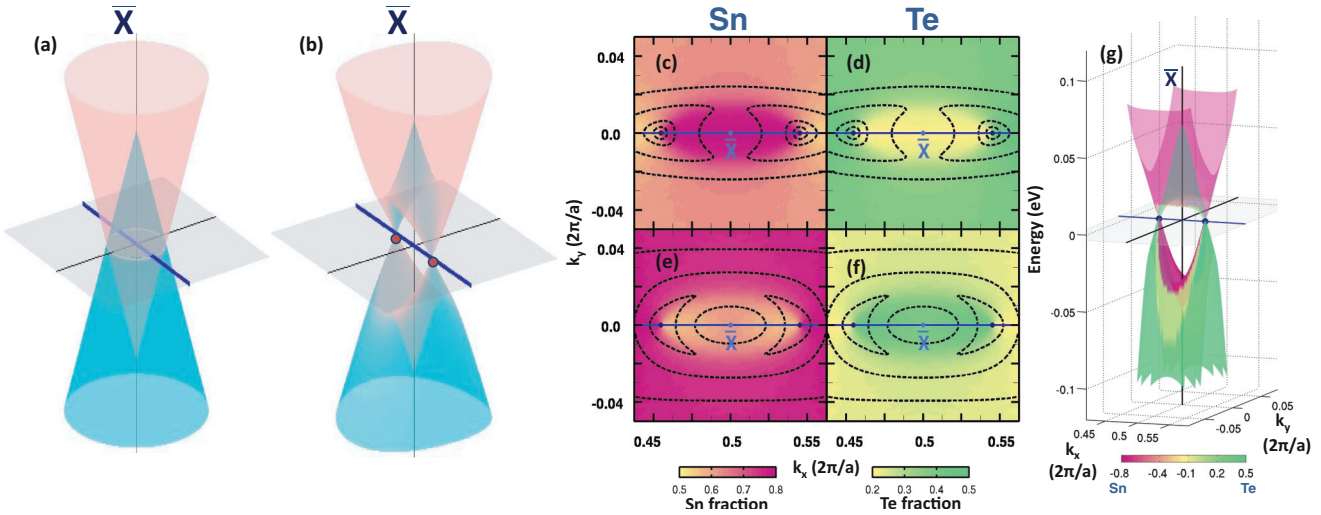

FIG. 2. (Color online) Two interacting coaxial Dirac cones. Schematic diagram for a noninteracting and interacting coaxial Dirac cone centered at the $\bar{X}$ point is shown in (a) and (b), respectively. As the interaction between the two Dirac cones is turned on, gaps open up except at the two new Dirac points on the two sides of the $\bar{X}$ point. The new gapless Dirac cones are protected by the presence of the mirror plane which intersects the surface BZ along $\bar{\Gamma}\bar{X}$ (bold blue line). Maps of the fraction of the partial charges on Sn and Te atoms for the valence surface bands are shown in (c) and (d), respectively, while those for the conduction surface bands are shown in (e) and (f). Dashed lines are the constant energy contours. (g) Surface band dispersion with colors indicating the fraction of partial charges on the Sn and Te atoms.

centered at the $\bar{X}$ point are associated with the Sn-like upper Dirac cone and the Te-like lower Dirac cone, respectively.

It is interesting to see how the spin textures within our picture of two coaxial Dirac cones play out based on the spin textures derived from our first-principles computations. Note that for the conduction bands shown in Fig. 3(a), the spin texture shows counterclockwise rotation around the $\bar{X}$ point and clockwise rotation far away from the $\bar{X}$ point. As shown in the schematic diagram of Fig. 3(c), states near the $\bar{X}$ point are associated with the Te-like lower Dirac cone, while those far away from the $\bar{X}$ point belong to the Sn-like upper Dirac cone. The two coaxial cones therefore should mimic similar chirality. They should both have clockwise spin rotation in the upper cone and counterclockwise in the lower cone. Along the $\bar{\Gamma}\bar{X}$ direction, these two opposite spin states meet at the Dirac points. Along the $\bar{X}\bar{M}$ direction, the spin polarization diminishes and switches direction around the Lifshitz transition. The spin texture of the valence surface states can be understood along similar lines. A clockwise rotation in the inner region around $\bar{X}$ is associated with the Sn-like upper Dirac cone, while a counterclockwise rotation in the outer region far away from the $\bar{X}$ point is associated with the Te-like lower Dirac cone. We note that the spin chirality of the surface Dirac cone in a typical strong topological insulator like Bi_2Se_3 (Ref. 7) is the same as that of the Sn-like and Te-like Dirac cones we have found here on the surface of SnTe, and bears a nontrivial mirror Chern number further discussed below.

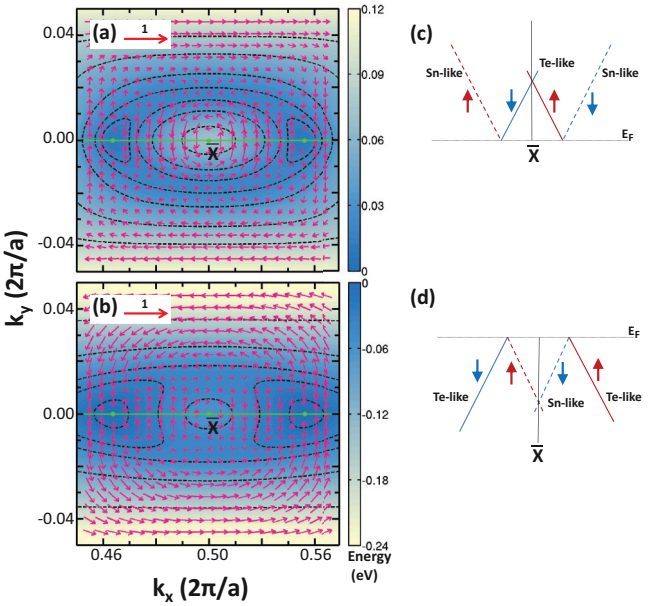

FIG. 3. (Color online) Nontrivial spin texture of SnTe surface states. Spin textures of the conduction and valence surface bands are shown in (a) and (b), respectively. Energy is represented by the color scale, and constant energy contours are shown. Green line indicates the $\bar{\Gamma}\bar{X}$ direction and green dots denote the Dirac points. Schematic band structures for the conduction and valence surface bands along the $\bar{\Gamma}\bar{X}$ direction are shown in (c) and (d), respectively. Solid lines are Te-like Dirac cones, and the dashed lines are Sn-like. Red (blue) arrows indicate the spin along positive (negative) y direction.

III. SIMPLIFIED k · p MODEL

In order to make our proposed two-coaxial-cone picture more concrete, we now discuss a 2D $\mathbf{k}\cdot\mathbf{p}$ model, which not only captures correctly the evolution in band dispersion under a Lifshitz transition, but also describes the spin texture reasonably.[20,21] In this connection, it is natural to consider a minimal four-band model with Hamiltonian $H(k_x,k_y)$ around the $\bar{X}$ point on the [001] surface that obeys the following three symmetries: mirror symmetry about

the xz plane (M_{xz}), mirror symmetry about the yz plane (M_{yz}), and time-reversal symmetry ($\Theta = TK$, where K denotes a complex conjugate). We then have under these symmetry operations, $M_{xz}H(k_x,k_y)M_{xz}^{-1} = H(k_x,-k_y)$, $M_{yz}H(k_x,k_y)M_{yz}^{-1} = H(-k_x,k_y)$, and $TH(k_x,k_y)T^{-1} = H^*(-k_x,-k_y)$.

As shown in Fig. 2(a), two distinct Dirac points occur at $\bar{X}$, associated with energies $E_+ > E_0$ and $E_- < E_0$. [E_0 denotes the energy level at which the two cones intersect.] To account for the doublet state at each Dirac point, we choose the basis set to be the eigenvectors of M_{yz} with eigenvalues $\pm i$: $\{|i;\mathrm{Sn}\rangle, |-i;\mathrm{Sn}\rangle, |-i;\mathrm{Te}\rangle, |i;\mathrm{Te}\rangle\}$, where the main atomic portion for each cone is indicated. In particular, when combined with the dominant orbitals for Sn (p_z) and Te (p_x) atoms mentioned earlier, this basis set also captures spin information, resulting in $\{|p_z,\rightarrow;\mathrm{Sn}\rangle, |p_z,\leftarrow;\mathrm{Sn}\rangle, |p_x,\rightarrow;\mathrm{Te}\rangle, |p_x,\leftarrow;\mathrm{Te}\rangle\}$. Note that the quantization axis for spin is now along x, with $M_{yz}|p_z,\rightarrow(\leftarrow)\rangle = \pm i|p_z,\rightarrow(\leftarrow)\rangle$ and $M_{yz}|p_x,\rightarrow(\leftarrow)\rangle = \mp i|p_x,\rightarrow(\leftarrow)\rangle$. Defining 4×4 matrices, $\Sigma_{\alpha\beta} = s_\alpha \otimes \sigma_\beta$, with Pauli matrices $\mathbf{s}$ and σ acting on spin and orbital spaces, respectively, the symmetry operator M_{yz} then takes the form $i\Sigma_{33}$, and the other two symmetry operators can be written as $M_{xz} = -i\Sigma_{20}$ and $T = -i\Sigma_{20}$. After examining the 16 Σ matrices under all three symmetry operations, up to linear coupling in k_x, k_y, we obtain the following symmetry-allowed Hamiltonian:

$$\begin{aligned} H(\vec{k}) = {} & m\Sigma_{03} + m'\Sigma_{22} \\ & + k_x(v_{1x}\Sigma_{20} + v_{2x}\Sigma_{02} + v_{3x}\Sigma_{23}) \\ & + k_y(v_{1y}\Sigma_{30} + v_{2y}\Sigma_{11} + v_{3y}\Sigma_{33}). \end{aligned} \quad (1)$$

In Fig. 2(b), we plot the energy dispersions based on this effective Hamiltonian, which is clearly seen to capture the key features of first-principles calculations [see Fig. 2(g)]. The presence of two new Dirac points is due to the double degeneracy given by different M_{xz} eigenvalues and is thus protected by the mirror symmetry of the system about the xz plane, in sharp contrast to the Dirac points at $\bar{X}$, which are mainly protected by the time-reversal symmetry. As to the spin texture, note that $\langle s_3\rangle$ and $\langle s_2\rangle$ now represent the in-plane spin x and y components, respectively. Furthermore, one can prove that for any eigenstate with momentum $\mathbf{k}$, $\langle\mathbf{k}|s_1|\mathbf{k}\rangle = 0$ (out-of-plane component), as required by the combined TRS and the two mirror symmetries: $\langle\mathbf{k}|s_1|\mathbf{k}\rangle = \langle\mathbf{k}|M_{xz}M_{yz}\Theta s_1\Theta^{-1}M_{yz}^{-1}M_{xz}^{-1}|\mathbf{k}\rangle = -\langle\mathbf{k}|s_1|\mathbf{k}\rangle$. It turns out that the resulting spin texture is qualitatively similar to that shown in Fig. 3. Finally, we note that if one applies a unitary transformation, $U = e^{i\frac{\pi}{4}s_2}\otimes\sigma_0$, to Eq. (1), the transformed $H(\vec{k})$ becomes

$$\tilde{H}(\vec{k}) = \begin{pmatrix} m & -iv_{x+}k_x - v_{y+}k_y & -iv_{2x}k_x + v_{2y}k_y & -m' \\ iv_{x+}k_x - v_{y+}k_y & m & m' & -iv_{2x}k_x - v_{2y}k_y \\ iv_{2x}k_x + v_{2y}k_y & m' & -m & -iv_{x-}k_x - v_{y-}k_y \\ -m' & iv_{2x}k_x - v_{2y}k_y & iv_{x-}k_x - v_{y-}k_y & -m \end{pmatrix}, \quad (2)$$

where $v_{x\pm} = v_{1x} \pm v_{3x}$ and $v_{y\pm} = v_{1y} \pm v_{3y}$. This is in fact a more familiar Hamiltonian, representing two interacting Dirac cones in the Rashba form, $\mathbf{k}\times\mathbf{s}$, with an identical chirality.[22,23] In Table I we list the parameter sets used in Eq. (2), obtained by fitting experimental angle-resolved photoemission spectroscopy (ARPES) band dispersions in topologically nontrivial (Pb,Sn)Te,[10] SnTe,[11,24] and (Pb,Sn)Se.[12,25,26]

TABLE I. Parameter sets for the 2D $\mathbf{k}\cdot\mathbf{p}$ model Hamiltonian of Eq. (2) obtained by fitting the experimental ARPES band dispersions in (Pb,Sn)Te,[10] SnTe,[11,24] and (Pb,Sn)Se.[12,25,26] $\{m, m'\}$, are given in units of electronvolts, and $\{v_{x\pm}, v_{2x}, v_{y\pm}, v_{2y}\}$ in units of eV·Å.

	$Pb_{1-x}Sn_xTe$		$Pb_{1-x}Sn_xSe$	
	$x = 0.4$	SnTe	$x = 0.23$	$x = 0.3$
m	–0.30	–0.30	–0.052	–0.056
m'	–0.15	–0.15	–0.042	–0.026
v_{x+}	–2.3	–2.3	–2.3	–2.58
v_{x-}	–2.3	–2.3	–3.5	–2.58
v_{2x}	0.0	0.0	–0.6	–0.32
$v_{y\pm}$	–5	–6.5	–3.85	–3.28
v_{2y}	0	0	0	0

IV. DISCUSSION AND CONCLUSION

In general, topological crystalline insulators should harbor distinct classes with positive and negative mirror Chern numbers. The schematic diagrams of possible spin textures around the lower Dirac cones are given in Fig. 4. In Fig. 4(a), a pair of Dirac cones with counterclockwise spin texture on the horizontal mirror line gives the mirror Chern number $n_m = -2$. The opposite case with a clockwise spin texture in Fig. 4(b) would give the mirror Chern number $n_m = 2$. By comparing the spin texture obtained from our first-principles calculations in Fig. 3, we can conclude that the mirror Chern number of SnTe is -2. For the Bi_2Se_3 system shown in Fig. 4(c), on a mirror line, only a single Dirac cone appears at the center of the hexagonal Brillouin zone with the mirror Chern number $n_m = -1$. In Fig. 4(d), if the spin texture runs clockwise, the system has the mirror Chern number $n_m = 1$. Since there are two coaxial Dirac cones in SnTe, where the Sn-like and Te-like Dirac cones exhibit the same spin chirality as Bi_2Se_3, it follows that the mirror Chern number of SnTe is twice that of Bi_2Se_3.

In conclusion, we have delineated the charge density distributions and spin textures of the [001] surface states on the topological crystalline insulator SnTe via first-principles

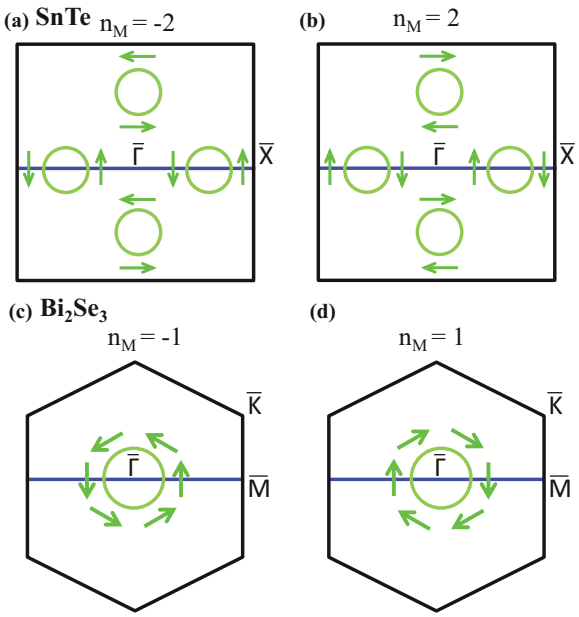

FIG. 4. (Color online) Schematic diagrams for spin textures of the lower Dirac cones in distinct topological phases associated with various values of the mirror Chern number n_m: (a) $n_m = -2$; (b) $n_m = 2$; (c) $n_m = -1$; and (d) $n_m = 1$. Blue lines indicate the axis of mirror symmetry.

calculations. We show that the SnTe surface states can be pictured as two interacting coaxial Dirac cones which intersect each other to form the Dirac points along the mirror symmetry line $\bar{\Gamma}\bar{X}$. From an examination of the charge distribution, we attribute the origin of the two coaxial Dirac cones to the two distinct atomic species, Sn and Te, in the material. The crystal and time-reversal symmetries guarantee that the out-of-plane spin polarization is zero. The spin texture is dictated by the nontrivial Chern number $n_m = -2$ in SnTe, which is different from the known Z_2 topological insulators such as Bi_2Se_3.

ACKNOWLEDGMENTS

It is a pleasure to thank Liang Fu and Chen Fang for useful discussions. The work at Northeastern and Princeton is supported by the Division of Materials Science and Engineering, Basic Energy Sciences, US Department of Energy, Grants No. DE-FG02-07ER46352, No. DE-FG-02-05ER46200, and No. AC02-05CH11231, and benefited from theory support at the Advanced Light Source, Berkeley, and the allocation of supercomputer time at NERSC and Northeastern University's Advanced Scientific Computation Center (ASCC). W.F.T. is supported by the NSC in Taiwan under Grant No. 100-2112-M-110-001-MY2.

[1] M. Z. Hasan and C. L. Kane, Rev. Mod. Phys. **82**, 3045 (2010).
[2] X.-L. Qi and S.-C. Zhang, Rev. Mod. Phys. **83**, 1057 (2011).
[3] M. Z. Hasan and J. E. Moore, Annu. Rev. Condens. Matter Phys. **2**, 5578 (2011).
[4] M. Konig, H. Buhmann, L. W. Molenkamp, T. Hughes, C-X. Liu, X-L. Qi, and S-C. Zhang, J. Phys. Soc. Jpn. **77**, 031007 (2008).
[5] L. Fu and C. L. Kane, Phys. Rev. B **76**, 045302 (2007).
[6] D. Hsieh, D. Qian, L. Wray, Y. Xia, Y. S. Hor, R. J. Cava, and M. Z. Hasan, Nature (London) **452**, 970 (2008).
[7] D. Hsieh, Y. Xia, D. Qian, L. Wray, J. H. Dil, F. Meier, J. Osterwalder, L. Patthey, J. G. Checkelsky, N. P. Ong, A. V. Fedorov, H. Lin, A. Bansil, D. Grauer, Y. S. Hor, R. J. Cava, and M. Z. Hasan, Nature (London) **460**, 1101 (2009).
[8] L. Fu, Phys. Rev. Lett. **106**, 106802 (2011).
[9] T. H. Hsieh, H. Lin, J. Liu, W. Duan, A. Bansil, and L. Fu, Nat. Commun. **3**, 982 (2012).
[10] S.-Y. Xu, C. Liu, N. Alidoust, M. Neupane, D. Qian, I. Belopolski, J. D. Denlinger, Y. J. Wang, H. Lin, L. A. Wray, G. Landolt, B. Slomski, J. H. Dil, A. Marcinkova, E. Morosan, Q. Gibson, R. Sankar, F. C. Chou, R. J. Cava, A. Bansil, and M. Z. Hasan, Nat. Commun. **3**, 1192 (2012).
[11] Y. Tanaka, Z. Ren, T. Sato, K. Nakayama, S. Souma, T. Takahashi, K. Segawa, and Y. Ando, Nat. Phys. **8**, 800 (2012).
[12] P. Dziawa, B. J. Kowalski, K. Dybko, R. Buczko, A. Szczerbakow, M. Szot, E. Usakowska, T. Balasubramanian, B. M. Wojek, M. H. Berntsen, O. Tjernberg, and T. Story, Nature Mater. **11**, 1023 (2012).
[13] J. C. Y. Teo, L. Fu, and C. L. Kane, Phys. Rev. B **78**, 045426 (2008).
[14] Following common practice, symmetry points in the *surface* Brillouin zone are denoted with a bar on the symbol (e.g., $\bar{\Gamma}$), while the symmetry points in the 3D Brillouin zone are denoted without a bar.
[15] R. Takahashi and S. Murakami, Phys. Rev. Lett. **107**, 166805 (2011).
[16] G. Kresse and D. Joubert, Phys. Rev. B **59**, 1758 (1999).
[17] J. P. Perdew, K. Burke, and M. Ernzerhof, Phys. Rev. Lett. **77**, 3865 (1996).
[18] G. Kresse and J. Hafner, Phys. Rev. B **48**, 13115 (1993).
[19] R. F. Bis and J. R. Dixon, J. Appl. Phys. **40**, 1918 (1969).
[20] C. Fang *et al.*[21] considered a similar approach but without any spin information.
[21] C. Fang, M. J. Gilbert, S.-Y. Xu, B. A. Bernevig, and M. Z. Hasan, arXiv:1212.3285.
[22] The picture of two degenerate Dirac cones given in the recent work by J. Liu *et al.*[23] can be obtained via a unitary transformation of our Hamiltonian, and is thus equivalent to our $\mathbf{k} \cdot \mathbf{p}$ model.
[23] J. Liu, W. Duan, and L. Fu, arXiv:1304.0430.
[24] Y. Tanaka, T. Sato, K. Nakayama, S. Souma, T. Takahashi, Z. Ren, M. Novak, K. Segawa, and Y.Ando, Phys. Rev. B **87**, 155105 (2013).
[25] Parameters listed in the 4th column in Table I for $Pb_{0.77}Sn_{0.23}Se$ are based on a corrected version of the ARPES spectra in Fig. 3 of Ref. 12, which has been communicated privately to us by the authors of Ref. 12.
[26] M. Neupane, S.-Y. Xu, Q. Gibson, Y. J. Wang, N. Alidoust, C. Liu, I. Belopolski, S. Basak, W.-F. Tsai, H. Lin, R. Sankar, A. Bansil, F. C. Chou, R. J. Cava, and M. Z. Hasan (in preparation).